

Interferometric modeling of wave propagation in inhomogeneous elastic media using time reversal and reciprocity

Dirk-Jan van Manen¹, Andrew Curtis², and Johan O. A. Robertsson³

ABSTRACT

Time reversal of arbitrary, elastodynamic wavefields in partially open media can be achieved by measuring the wavefield on a surface surrounding the medium and applying the time reverse of those measurements as a boundary condition. We use a representation theorem to derive an expression for the time-reversed wavefield at arbitrary points in the interior. When this expression is used to compute, in a second point, the time-reversed wavefield originating from a point source, the time-reversed Green's function between the two points is observed. By invoking reciprocity, we obtain an expression that is suitable for modeling of wave propagation through the medium. From this we develop an efficient and flexible two-stage modeling scheme. In the initial phase, the model is illuminated systematically from a surface surrounding the medium using a sequence of conventional forward-modeling runs. Full waveforms are stored for as many points in the interior as possible. In the second phase, Green's functions between arbitrary points in the volume can be computed by crosscorrelation and summation of data computed in the initial phase. We illustrate the method with a simple acoustic example and then apply it to a complex region of the elastic Pluto model. It is particularly efficient when Green's functions are desired between a large number of points, but where there are few common source or receiver points. The method relies on interference of multiply scattered waves, but it is stable. We show that encoding the boundary sources using pseudonoise sequences and exciting them simultaneously, akin to daylight imaging, is inefficient and in all explored cases leads to relatively high-noise levels.

INTRODUCTION

Many applications in diverse fields such as communications anal-

ysis, waveform inversion, imaging, survey and experimental design, and industrial design require a large number of modeled solutions of the wave equation in different media. The most complete methods of solution, such as finite differences (FD), which model accurately all high-order interactions between scatterers in a medium, typically become prohibitively expensive for realistically complete descriptions of the medium and geometries of sources and receivers, and hence, for solving realistic problems based on the wave equation. Recently, van Manen et al. (2005) showed that the key to breaking this apparent paradigm lies in combining a basic reciprocity argument with contemporary theoretical advances in the fields of time-reversed acoustics (Derode et al., 2003) and seismic interferometry (Schuster, 2001; Weaver and Lobkis, 2001; Wapenaar, 2004).

In time-reversed acoustics, the invariance of the wave equation to time reversal is exploited to focus a wavefield through a highly scattering medium on an original source point (Derode et al., 1995). Cassereau and Fink (1992, 1993) realized that an acoustic representation theorem can be used to time-reverse a wavefield in a volume by creating secondary sources on a surface surrounding the medium such that the boundary conditions correspond to the time-reversed components of a wavefield measured there. These secondary sources give rise to the back-propagating, time-reversed wavefield inside the medium that collapses onto itself at the original source location. Note that because there is no source term absorbing the converging wavefield, the size of the focal spot is limited to half a (dominant) wavelength in accordance with diffraction theory (Cassereau and Fink, 1992). The diffraction limit was overcome experimentally by de Rosny and Fink (2002) by introducing the concept of an acoustic sink.

In interferometry, waves recorded at two receiver locations are correlated to find the Green's function between the locations. Interferometry has been applied successfully to helioseismology (Rickett and Claerbout, 2000), ultrasonics (Weaver and Lobkis, 2001), and exploration seismics (Bakulin and Calvert, 2004, 2006; Wapenaar et

Manuscript received by the Editor May 25, 2005; revised manuscript received December 2, 2005; published online August 17, 2006.

¹University of Edinburgh, School of GeoSciences, Grant Institute, West Mains Road, Edinburgh EH9 3JW, United Kingdom and WesternGeco Oslo Technology Centre, Solbraveien 23, 1383, Norway. E-mail: dmanen@oslo.westerngeco.slb.com.

²University of Edinburgh, School of GeoSciences, Grant Institute, West Mains Road, Edinburgh EH9 3JW, United Kingdom. E-mail: andrew.curtis@ed.ac.uk.

³WesternGeco Oslo Technology Centre, Solbraveien 23, 1383, Norway. E-mail: jrobertsson@oslo.westerngeco.slb.com.

© 2006 Society of Exploration Geophysicists. All rights reserved.

al., 2004). Recently, it was shown that there exists a close link between the time-reversed acoustics and interferometry disciplines when Derode et al. (2003) analyzed the emergence of the Green's function from field-field correlations in an open scattering medium in terms of time-reversal symmetry. The Green's function can be recovered as long as the sources in the medium are distributed, forming a perfect time-reversal device.

Here, we extend the interferometric-modeling method of van Manen et al. (2005) to elastic media and show how the theorem by Derode et al. (2003) can be derived from an elastodynamic representation theorem. We demonstrate the connection with the Porter-Bojarski equation in the field of generalized holography in optics (Porter, 1969, 1970; Bojarski, 1983) and reciprocity theorems of the correlation type (de Hoop, 1988, 1995; Fokkema and van den Berg, 1993; Wapenaar et al., 2004). More specifically, we show how the elastodynamic representation theorem can be used to time reverse a wavefield in a volume and how, using the appropriate sets of Green's functions, the time-reversed wavefield can be computed at any point in the interior. Note that the elastodynamic Kirchhoff integral has previously been used as a boundary condition in reverse-time FD migration (Mittet, 1994; Hokstad et al., 1998) and in the FD injection method proposed by Robertsson and Chapman (2000) to compute efficiently FD seismograms after model alterations. By applying a simple reciprocity argument, it is shown how the elastodynamic Green's tensor between arbitrary points in a volume can be computed using only crosscorrelations and numerical integration once the Green's tensors from sources on the surrounding surface to these points are known. Illuminating a model from the outside thus leads to a flexible and efficient modeling algorithm.

The method is first illustrated using a simple acoustic model consisting of isotropic point scatterers embedded in a homogeneous background medium. This is followed by an example for a more complicated, inhomogeneous, elastic medium and a detailed discussion of computational aspects. The limits of using pseudonoise sources on the boundary and exciting them simultaneously are discussed also. Finally, we speculate about reducing the number of sources on the surrounding surface as a way of approximate modeling that maintains high-order scattering and suggest possible synergies with methods of inversion for medium properties.

In the next section, the interferometric modeling method will be derived from the elastodynamic representation theorem, closely following the physically intuitive reasoning of Derode et al. (2003). However, to understand fully the relation between time reversal, interferometry, and generalized holography, it is useful briefly to review reciprocity.

RECIPROCITY AND THE REPRESENTATION THEOREM

A reciprocity theorem relates two independent, acoustic, electromagnetic or elastodynamic states that can occur in the same spatiotemporal domain, where a state simply means a combination of material parameters, field quantities, source distributions, boundary conditions, and initial conditions that satisfy the relevant wave equation. In its most general form, it relates a specific combination of field quantities from both states on a surface surrounding a volume to differences in source distributions, medium parameters, boundary conditions, or even flow velocities (in cases where the material is moving) throughout the volume (Fokkema and van den Berg, 1993; de Hoop, 1995; Wapenaar and Fokkema, 2004).

Here, we consider a special case of elastodynamic reciprocity where the medium in both states is identical and nonflowing. In that case, states (A) and (B) are characterized simply by the following wave equations (in the space-frequency domain):

$$\rho\omega^2 u_i^{(A)} + \partial_j(c_{ijkl}\partial_k u_l^{(A)}) = -f_i^{(A)}, \quad (1)$$

$$\rho\omega^2 u_i^{(B)} + \partial_j(c_{ijkl}\partial_k u_l^{(B)}) = -f_i^{(B)}, \quad (2)$$

where $u_i^{(A)}$ and $u_i^{(B)}$ denote the components of particle displacement for state (A) and (B), respectively, generated by the components of body-force density $f_i^{(A)}$ and $f_i^{(B)}$, and where $c_{ijkl}(\mathbf{x})$ and $\rho(\mathbf{x})$ are the stiffness tensor and mass density, respectively, at location \mathbf{x} in the medium. Note that Einstein's summation convention for repeated indices is used. The Betti-Rayleigh reciprocity theorem can be derived by multiplying the first equation by $u_i^{(B)}$ and the second by $u_i^{(A)}$, subtracting the results, integrating over a volume V , and using Gauss' theorem to convert volume integrals to surface integrals. This gives (Snieder, 2002)

$$\begin{aligned} & \int_S \{u_i^{(B)} n_j c_{ijkl} \partial_k u_l^{(A)} - n_j c_{ijkl} \partial_k u_l^{(B)} u_i^{(A)}\} dS \\ &= - \int_V \{f_i^{(A)} u_i^{(B)} - f_i^{(B)} u_i^{(A)}\} dV. \end{aligned} \quad (3)$$

Equation 3 is called a reciprocity theorem of the convolution type, because the displacement and traction from the two states multiply each other (Bojarski, 1983; de Hoop, 1988). A Betti-Rayleigh reciprocity theorem of the correlation type can be derived by taking the complex conjugate of both sides of equation 1:

$$\rho\omega^2 u_i^{*(A)} + \partial_j(c_{ijkl}\partial_k u_l^{*(A)}) = -f_i^{*(A)}, \quad (4)$$

where a star * denotes complex conjugation, and following the same procedure that led up to equation 3. This gives

$$\begin{aligned} & \int_S \{u_i^{(B)} n_j c_{ijkl} \partial_k u_l^{*(A)} - n_j c_{ijkl} \partial_k u_l^{(B)} u_i^{*(A)}\} dS \\ &= - \int_V \{f_i^{*(A)} u_i^{(B)} - f_i^{(B)} u_i^{*(A)}\} dV, \end{aligned} \quad (5)$$

where now the quantities from both states occur in pairs that correspond to crosscorrelation in the time domain. The physical significance of a reciprocity theorem of the correlation type will be discussed in detail below.

A representation integral can be derived from equation 3 by identifying one state with a mathematical or Green's state (i.e., a state where the source is a unidirectional point force and the resulting particle displacement is called the elastodynamic Green's function) and the other with a physical state that can be any wavefield resulting from an arbitrary source distribution. Thus, we arbitrarily choose state (B) to be the Green's state and take $\mathbf{f}^{(B)}$ a unit point force at location \mathbf{x}' in the n direction: $f_i^{(B)}(\mathbf{x}) = \delta_{in} \delta(\mathbf{x} - \mathbf{x}')$, where δ_{in} and $\delta(\mathbf{x})$ denote the Kronecker symbol and Dirac distribution, respectively, and the wavefield $u_i^{(B)}(\mathbf{x})$ becomes the Green tensor: $u_i^{(B)}(\mathbf{x}) = G_{in}(\mathbf{x}, \mathbf{x}')$. We leave state (A), unspecified. Inserting these expressions into equation 3, carrying out the volume integral, dropping the superscripts for state (A), and making no assumptions about the boundary conditions, we arrive at

$$u_n(\mathbf{x}') = \int_V G_{in}(\mathbf{x}, \mathbf{x}') f_i(\mathbf{x}) dV + \int_S \{G_{in}(\mathbf{x}, \mathbf{x}') n_j c_{ijkl} \partial_k u_l(\mathbf{x}) - n_j c_{ijkl} \partial_k G_{in}(\mathbf{x}, \mathbf{x}') u_l(\mathbf{x})\} dS. \quad (6)$$

Finally, applying reciprocity to the Green's tensor and allowing the exchange of coordinates $\mathbf{x} \leftrightarrow \mathbf{x}'$ and indices $i \leftrightarrow n$, we arrive at the elastodynamic representation theorem (Snieder, 2002)

$$u_i(\mathbf{x}) = \int_V G_{in}(\mathbf{x}, \mathbf{x}') f_n(\mathbf{x}') dV' + \int_S \{G_{in}(\mathbf{x}, \mathbf{x}') n_j c_{njkl} \partial'_k u_l(\mathbf{x}') - n_j c_{njkl} \partial'_k G_{il}(\mathbf{x}, \mathbf{x}') u_n(\mathbf{x}')\} dS', \quad (7)$$

where $\partial'_k G_{il}(\mathbf{x}, \mathbf{x}')$ denotes the partial derivative of the Green's tensor in the k direction with respect to primed coordinates, and \mathbf{n} denotes the normal to the boundary. Thus, the wavefield $u_i(\mathbf{x})$ can be computed everywhere inside the volume V once the exciting force $f_n(\mathbf{x}')$ inside the volume and the displacement $u_n(\mathbf{x}')$ and the associated traction $n_j c_{ijkl} \partial'_k u_l(\mathbf{x}')$ on the surrounding surface S are known.

TIME REVERSAL USING THE REPRESENTATION THEOREM

To time-reverse a wavefield in a volume V , one possibility would be to reverse the particle velocity at every point inside the volume simultaneously. However, Cassereau and Fink (1992) noted that for open systems (i.e., with outgoing boundary conditions on at least part of the surrounding surface S), time reversal can be achieved also by measuring the wavefield and its gradient on the enclosing surface, time-reversing those measurements, and letting them act as a time-varying boundary condition on the surface S . Their approach directly follows from an application of Green's theorem (or the Kirchhoff-Helmholtz integral) and is easily extended to elastodynamic-wave propagation using equation 7, derived above. Thus, to time-reverse any wavefield $u_i(\mathbf{x})$, resulting from an arbitrary source distribution $f_n(\mathbf{x})$, we substitute the complex conjugate of the wavefield (phase conjugation being equivalent to time reversal), its gradient, and its sources into the elastodynamic representation theorem (equation 7). This gives

$$u_i^*(\mathbf{x}) = \int_V G_{in}(\mathbf{x}, \mathbf{x}') f_n^*(\mathbf{x}') dV' + \int_S \{G_{in}(\mathbf{x}, \mathbf{x}') n_j c_{njkl} \partial'_k u_l^*(\mathbf{x}') - n_j c_{njkl} \partial'_k G_{il}(\mathbf{x}, \mathbf{x}') u_n^*(\mathbf{x}')\} dS'. \quad (8)$$

Equation 8 can be used to compute the back-propagating wavefield (including all high-order interactions) at any location, not just at an original-source location. It can be confirmed also that equation 8 is a valid representation for the time-reversed wavefield by substituting two forward Green's states into the equivalent Betti-Rayleigh reciprocity theorem of the correlation type (equation 5).

In order for the time reversal to be complete, the energy converging at the original source locations should be absorbed at the appropriate time. Thus, the volume integral in the right-hand side of equa-

tion 8 corresponds to the wavefield generated by a distribution of elastic sinks (de Rosny and Fink, 2002), which destructively interferes with the time-reversed wavefield that propagates through the foci.

Now, say that the wavefield $u_i(\mathbf{x})$ also was set up originally by a point-force source excitation, but at location \mathbf{x}'' and in the m direction [i.e., $f_i(\mathbf{x}) = \delta_{im} \delta(\mathbf{x} - \mathbf{x}'')$ and $u_i(\mathbf{x})$ is a Green's tensor: $u_i(\mathbf{x}) = G_{im}(\mathbf{x}, \mathbf{x}'')$]. Thus, if we compare equations 7 and 8, it is clear that effectively we are taking the unspecified state to be a time-reversed Green's state, which satisfies the conjugated wave equation $\rho \omega^2 G_{im}^* + \partial_j (c_{ijkl} \partial_k G_{im}^*) = -\delta_{im} \delta(\mathbf{x} - \mathbf{x}'')$ (cf. equation 4). Inserting these expressions in equation 8 and carrying out the volume integration gives

$$G_{im}^*(\mathbf{x}, \mathbf{x}'') = G_{im}(\mathbf{x}, \mathbf{x}'') + \int_S \{G_{in}(\mathbf{x}, \mathbf{x}') n_j c_{njkl} \partial'_k G_{lm}^*(\mathbf{x}', \mathbf{x}'') - n_j c_{njkl} \partial'_k G_{il}(\mathbf{x}, \mathbf{x}') G_{nm}^*(\mathbf{x}', \mathbf{x}'')\} dS'. \quad (9)$$

Equation 9 relates the time-advanced and time-retarded elastodynamic Green's functions. In the field of generalized holography in optics, an equation of this type is often referred to as the Porter-Bojarski equation after the work by Porter (1969, 1970) and Bojarski (1983), who previously derived it for the scalar, inhomogeneous, Helmholtz-wave equation and electric and magnetic vector wavefields.

Note that the time-retarded Green's function $G_{im}(\mathbf{x}, \mathbf{x}'')$ in the right-hand side now corresponds to the wavefield generated by the point-force elastic sink. In the following, the elastic sink will not be modeled — only the integral term in equation 9 will be calculated. Physically, this means that the converging wavefield will immediately start diverging again after focusing. Mathematically, the time-retarded Green's function must be subtracted from both sides of equation 9, and the homogeneous Green's function, $G_{im}^h(\mathbf{x}, \mathbf{x}'') \equiv G_{im}^*(\mathbf{x}, \mathbf{x}'') - G_{im}(\mathbf{x}, \mathbf{x}'')$, will be obtained: The time-reversed wavefield is a solution to the homogeneous wave equation (i.e., without a source term). The latter also follows immediately when subtracting the wave equations for the forward and time-reversed states (Oristaglio, 1989; Cassereau and Fink, 1992).

Equation 9 states that by measuring or computing the time-reversed wavefield at location \mathbf{x} for a source originally at location \mathbf{x}'' , the Green's function and its time reverse between the source point \mathbf{x}'' and point \mathbf{x} are observed. This agrees with other recent experimental and theoretical observations (Derode et al., 2003; Wapenaar, 2004). Using reciprocity, $G_{ij}(\mathbf{x}', \mathbf{x}) = G_{ji}(\mathbf{x}, \mathbf{x}')$, we can rewrite equation 9 so that it involves only sources on the boundary enclosing the medium:

$$G_{im}^*(\mathbf{x}, \mathbf{x}'') - G_{im}(\mathbf{x}, \mathbf{x}'') = \int_S \{G_{in}(\mathbf{x}, \mathbf{x}') n_j c_{njkl} \partial'_k G_{ml}^*(\mathbf{x}'', \mathbf{x}') - n_j c_{njkl} \partial'_k G_{il}(\mathbf{x}, \mathbf{x}') G_{mn}^*(\mathbf{x}'', \mathbf{x}')\} dS'. \quad (10)$$

Hence, the Green's function between two points \mathbf{x} and \mathbf{x}'' in a partially open, elastic medium can be calculated once the Green's functions between the enclosing boundary and each of these points are known. In the following, we refer to equation 10 as the interferometric-modeling equation.

INTERFEROMETRIC MODELING

A highly efficient, two-stage modeling strategy follows from equation 10: First, the Green's function terms $G_{im}(\mathbf{x}, \mathbf{x}')$ and $n_j c_{ijkl} \partial_l G_{im}(\mathbf{x}, \mathbf{x}')$ under the integral sign are calculated from boundary locations to internal points in a conventional forward-modeling phase; in a second intercorrelation phase, the integral is calculated, requiring only crosscorrelations and numerical integration. Because the computational cost of typical forward-modeling algorithms (e.g., FD) does not depend significantly on the number of receiver locations — but mainly on the number of source locations — efficiency and flexibility are achieved, because sources need only be placed around the bounding surface, not throughout the volume. The modeled wavefield should be stored for each of the boundary sources in as many points as possible throughout the medium. To calculate the components of the Green's tensor between two points, the appropriate components of the displacement vector in the first point, resulting from deformation-rate-tensor type sources on the boundary, are crosscorrelated with the appropriate components of the Green's tensor in the second point, resulting from the point-force sources from the same location on the boundary. The resulting crosscorrelation gathers are subtracted and numerically integrated over the boundary of source locations. Unprecedented flexibility follows from the fact that Green's functions can be calculated between all pairs of points that were previously defined and stored in the initial boundary-source modeling phase. Thus, we calculate a partial modeling solution that is common to all Green's functions, then a bespoke component for each Green's function. A flowchart of the interferometric-modeling method is given in Figure 1 and discussed in detail below for an acoustic, isotropic, point-scattering example.

Boundary conditions

Note that because of the symmetry of the terms in the integrand in equation 10, no sources are required along the earth's free surface, or

any interface with homogeneous boundary conditions (e.g., with vanishing traction or vanishing particle displacement). Intuitively, this can be understood from a method of imaging argument: Because such interfaces act as perfect mirrors, reflecting all energy back into the volume, an equivalent medium can be constructed that consists of the original medium combined with its mirror in the homogeneous boundary but with the homogeneous boundary absent. Because the original boundary with source locations is also mirrored, the new boundary completely surrounds this hypothetical medium; therefore, the sources constitute a perfect time-reversal mirror. Note that when the free surface has topography, although the method of imaging argument breaks down, this property still holds.

According to equation 10, derivatives of the Green's function with respect to the source location on the boundary also must be computed. As mentioned above, these terms correspond to the response caused by special (deformation-rate-tensor type) sources on the boundary and seem to require additional modeling with such special sources before Green's functions can be computed using the new method. However, using reciprocity, these terms also can be interpreted as the traction measured on the enclosing boundary resulting from point forces at a particular point of interest (cf. equation 8). Crosscorrelation of components of particle displacement with components of traction ensures that waves that are incoming and outgoing at the surrounding boundary are separated correctly in the correlation process (Wapenaar and Haimé, 1990; Mittet, 1994).

When part of the surface surrounding the medium has outgoing boundary conditions (i.e., no energy crosses the surface as ingoing wave), the displacement and the corresponding traction are related directly (Holvik and Amundsen, 2005).

In Appendix A, it is explained in detail how these properties can be exploited to avoid the need for additional direct modeling. When the boundary sources are embedded in a medium that is homogeneous along the source array, the components of the particle displacement in a particular point-of-interest gather are simply Fourier transformed into the frequency-wavenumber domain, matrix-multiplied with an analytical expression, and inverse-transformed back to the space-time domain. This directly gives the corresponding components of traction. When the boundary is curved or the medium is inhomogeneous along the source array, spatially compact filter approximations can be designed to filter the data in the space-frequency domain using space-variant convolution. Such an approach is used commonly to decompose multi-component seismic data into upgoing and downgoing waves in the shot domain and is described in detail in, e.g., Robertsson and Curtis (2002); Robertsson and Kragh (2002); van Manen et al. (2004); Amundsen et al. (2005).

Recently, Wapenaar et al. (2005) have shown, for the acoustic case, that when the surface surrounding the medium has outgoing boundary conditions, the two terms under the integral in the interferometric-modeling equation (equation 10) are approximately equal, but have opposite sign. In addition, when the surrounding surface has large enough radius such that Fraunhofer far-field (i.e., normal incidence) conditions apply, only monopole sources are required to compute Green's functions.

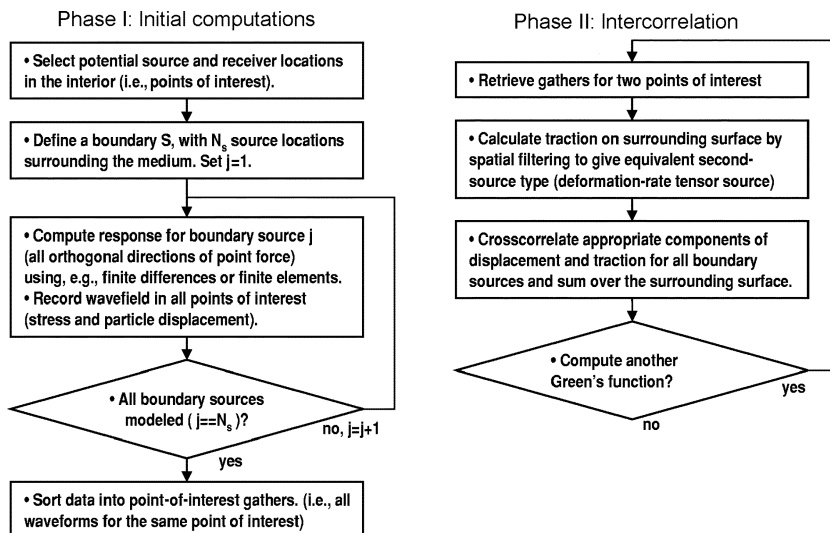


Figure 1. Flowchart of the proposed modeling method. The method consists of two main phases: an initial phase that creates a partial modeling solution that is common to all Green's functions (computed only once using a conventional forward-modeling algorithm), followed by a second phase where desired Green's functions are computed from the partial modeling solution using only crosscorrelation and summation, without the need for additional modeling.

Special case: Interferometric modeling of acoustic waves

The interferometric-modeling formula for acoustic waves can be derived similarly, as discussed in detail by van Manen et al. (2005). Here, we simply state their result, valid for partially open acoustic media (i.e., with outgoing, radiation, or absorbing boundary conditions on at least part of the surrounding surface):

$$G^*(\mathbf{x}, \mathbf{x}'') - G(\mathbf{x}, \mathbf{x}'') = \int_S \frac{1}{\rho(\mathbf{x}')} \{n_j \partial'_j G(\mathbf{x}, \mathbf{x}') G^*(\mathbf{x}'', \mathbf{x}') - G(\mathbf{x}, \mathbf{x}') n_j \partial'_j G^*(\mathbf{x}'', \mathbf{x}')\} dS', \quad (11)$$

where $G(\mathbf{x}, \mathbf{x}'')$ denotes the Green's function for the pressure at location \mathbf{x} resulting from a point source of volume injection at location \mathbf{x}'' , and $n_j \partial'_j G(\mathbf{x}, \mathbf{x}')$ denotes the normal derivative of Green's function with respect to primed coordinates. Thus, the pressure Green's function $G(\mathbf{x}, \mathbf{x}'')$ between two points \mathbf{x} and \mathbf{x}'' can be calculated once the Green's functions between the enclosing boundary and these points are known. Note that the terms $G(\mathbf{x}, \mathbf{x}')$ correspond to simple monopole sources on the surrounding surface, whereas the terms $n_j \partial'_j G(\mathbf{x}, \mathbf{x}')$ correspond to dipole sources. This formula will be used in the next section to compute the Green's function between points in a 2D acoustic model with three isotropic point scatterers embedded in a homogeneous background medium.

EXAMPLE 1: 2D ACOUSTIC ISOTROPIC POINT SCATTERING

The methodology described above is now explained in more detail using a simple 2D acoustic example. A more realistic elastic model, including strong heterogeneity and interfaces with homogeneous boundary conditions, is discussed in a later section. In Figure 2, three isotropic point scatterers are shown, embedded in a homogeneous background medium of infinite extent (background velocity $v_0 = 750$ m/s). The point scatterers are indicated by large black dots. The new method is used to model full-waveform Green's functions between arbitrary source and receiver locations in the medium.

As indicated in the flowchart in Figure 1, in the first step, a boundary enclosing the medium is defined and spanned by source locations. A large number of so-called *points of interest* are also specified. In Figure 2, every second boundary-source location is marked with a star. The boundary sources should be spaced according to local Nyquist criteria. The grid of small points are the points where we may be interested in placing a modeled source or receiver later. The number of points of interest should be chosen to be as large as possible, the only limitation being the waveform data-storage capacity. In Figure 2, the triangles denote some particular points of interest that we will be looking at later.

In the second step of the initial phase, separate, conventional, forward-modeling runs are carried out for each source on the boundary, and the wavefield is stored at all points of interest. In this example, we have used a deterministic variant of Foldy's method (Foldy, 1945; Groenenboom and Snieder, 1995; Snieder and Scales, 1998) to compute the multiply scattered wavefield for each boundary source. This method naturally incorporates radiation boundary conditions. Note that we could have used any method that accurately models multiple scattering (e.g., FD). Our methodology is not restricted to any particular forward-modeling method or code. Also,

because multiplication with a complex conjugate in the frequency domain corresponds to crosscorrelation in the time domain, the method is not limited to a frequency-domain implementation. In the following, the examples are computed using the time-domain equivalent of equation 11.

In Figure 2, a snapshot of the early stages of the wavefield is shown for the first source on the enclosing surface. Thus, in the second step, the interior of the model is illuminated systematically from the surrounding surface. During or after the simulations for all boundary sources, it is convenient to sort the data into point-of-interest gathers comprising data from all boundary sources recorded at each point of interest. These constitute a common component of all Green's functions involving that point of interest.

In the second intercorrelation phase, we now may calculate the Green's function between any pair of points that were defined beforehand by crosscorrelation and summation of boundary-source recordings. In Figure 2, the triangles denote a subset of points that we could be interested in as part of, e.g., a crosswell-survey design experiment.

In Figure 3a–d, the modeled wavefield resulting from each monopole source on the boundary is shown for two of the points of interest \mathbf{x}_1 and $b\mathbf{m}\mathbf{x}_2$ (with coordinates $[-50, 0]$ and $[50, -50]$, respectively). Note that even though there are only three isotropic point scatterers, several multiply scattered waves can be easily identified. Also, note the flat event at approximately $t = 0.2$ s. This is the incident wave from each boundary source, scattered isotropically in the direction of the two points of interest by the central scatterer (which is equidistant from each boundary source). In Figure 3b and c, the normal derivative with respect to the boundary has been computed by spatial filtering of the point-of-interest gathers (a) and (d), respectively, to simulate the response resulting from dipole sources on the boundary.

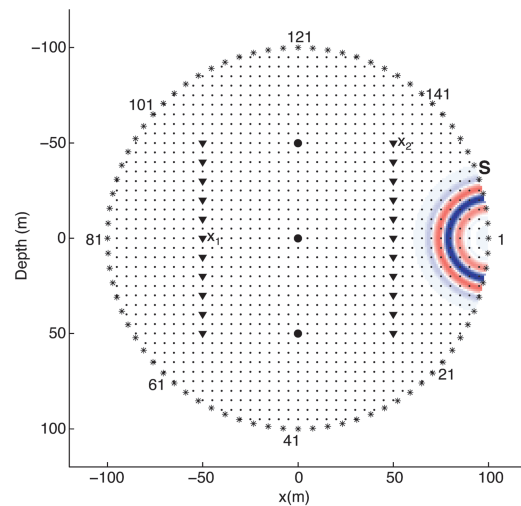


Figure 2. 2D acoustic model and snapshot of the first boundary-source wavefield: Three isotropic point scatterers (large black dots) embedded in a homogeneous background medium $v_0 = 750$ m/s of infinite extent. Stars (*) mark every second-source location on a surface enclosing the medium. Particular sources are numbered for reference with Figure 3a–f. Small dots (·) mark potential source and receiver locations (points of interest) for Green's-function intercorrelation. Triangles mark one of many crosswell-source/-receiver configurations that can be evaluated using the new method. In the initial phase, the wavefield is computed for all boundary sources separately and stored in all points of interest.

This is possible because we have outgoing (i.e., absorbing or radiation) boundary conditions on the surrounding surface, and hence the pressure and its gradient are related directly (see the section on boundary conditions and Appendix A for details). Calculation of the normal derivative with respect to the boundary-source location is completely equivalent to measuring the response resulting from a dipole source so; alternatively we could have modeled the required gradient using a second dipole-source type. Typically, however, direct modeling would be computationally much more expensive.

Figure 3e and f show the trace-by-trace crosscorrelation of panels (a) and (c), and (b) and (d), respectively. Thus, they form the two terms in the integrand of the time-domain equivalent of equation 11. It is difficult to make a straightforward interpretation of the crosscorrelation gathers: Although equation 11 predicts that the waveform resulting from summation of these crosscorrelations for all boundary sources will be antisymmetric in time, panels (e) and (f) clearly are not. This is because, at this stage, we still have not carried through the Huygens' summation (integration), which provides the

delicate (but stable) constructive and destructive interference of the back-propagating wavefield. It can be seen, as predicted by Wapenaar et al. (2005) and discussed in the section on boundary conditions, that Figure 3e and f are approximately equal, but have opposite sign. A more thorough analysis of the features of such crosscorrelation gathers is presented for the second example.

In the final step, crosscorrelation gathers of Figure 3e and f are weighted by ρ^{-1} , subtracted, and numerically integrated (summed) over all source locations. The resulting intercorrelation Green's function and a directly computed reference solution are shown in Figure 3g. The insets show particular events in the waveform in detail.

To further illustrate the new modeling method, the intercorrelation phase is now applied repeatedly to look up Green's functions for a simple crosswell-transmission- and reflection seismic experiment shown in Figure 2 (source and receiver locations are indicated by triangles). Note that this does not require any additional conventional forward modeling, but instead uses the same data modeled in the initial phase. Also, note that we could consider a

completely different well location, for any combination of points of interest (indicated by small dots in Figure 2), as long as they were defined beforehand and the wavefield was stored in those points during the initial modeling phase.

In Figure 4a and b, Green's functions computed using a conventional forward-modeling method and the new method are shown, respectively. These Green's functions correspond to the transmission experiment shown in Figure 2 (source at $[-50, -50]$, receivers distributed vertically from $[50, 50]$ to $[50, -50]$ at 1-m spacing). Note that the amplitudes have been scaled up to show the weak, multiply scattered events. In Figure 4c, the difference between the Green's functions computed with the two methods is shown, and the amplitude differences have been scaled up by a factor of 10 to emphasize the match. Similarly, in Figure 4d, c, and f, Green's functions computed using the new method are compared to a reference solution for the reflection setting shown in Figure 2 (source at $[-50, -50]$, receivers distributed vertically from $[-50, 50]$ to $[-50, -50]$ at 1-m spacing). Again, amplitude differences have been scaled up by a factor of 10. Note the mismatch in the Green's function for the direct wave close to the original-source location. This error results from the missing acoustic sink and the band-limited nature of the synthetic signals and agrees with the theory that predicts the diffraction-limited Green's function will be retrieved.

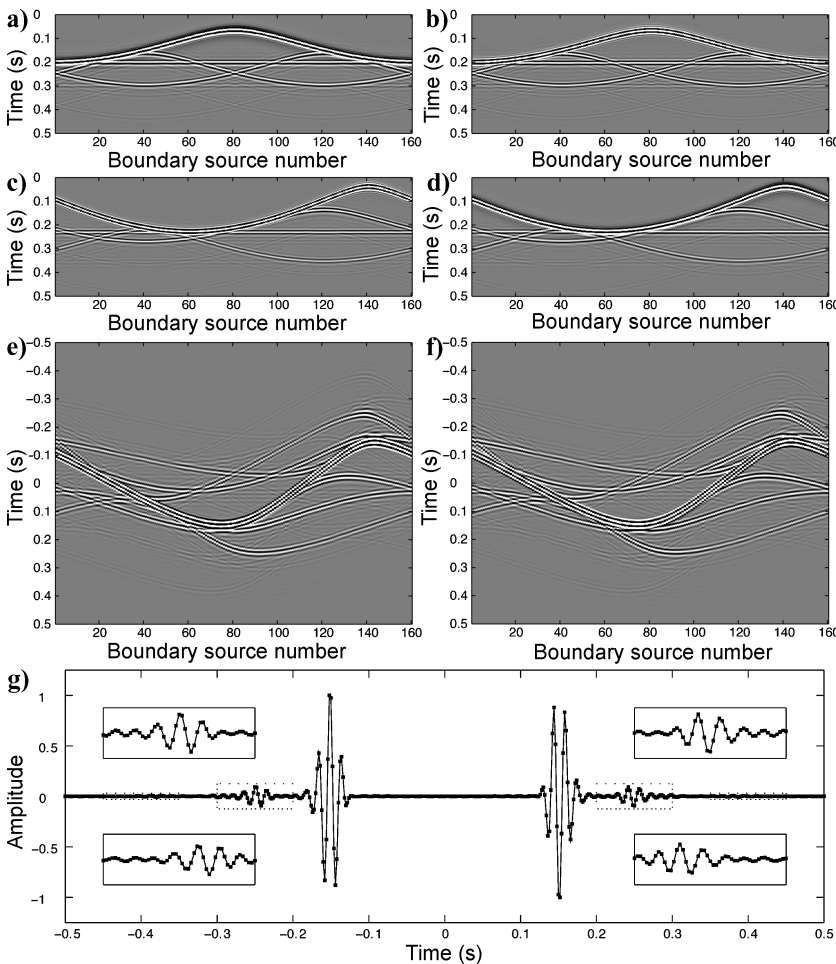


Figure 3. Modeled waveforms for all boundary sources in two points of interest and their crosscorrelation: (a) Monopole response in point x_1 , and (b) corresponding dipole response computed by spatial filtering (see text for details). (c) Dipole response in point x_2 computed by spatial filtering, and (d) corresponding monopole response. (e) Crosscorrelation of (a) and (c). (f) Crosscorrelation of (b) and (d). The difference between gathers (e) and (f), weighted by ρ^{-1} , forms the integrand of equation 11. (g) Intercorrelation Green's function (solid line) and a directly computed reference solution (squares). Insets show details of the signals in time intervals bounded by dashed boxes. Note the antisymmetry of the intercorrelation Green's function across $t = 0$ s, as predicted by equation 11.

EXAMPLE 2: 2D ELASTIC PLUTO MODEL

In the second example, we apply the method to an elastic model that is more relevant to the exploration seismic setting. In Figure 5, the compressional-wave velocity in a 4.6×4.6 -km region of the elastic Pluto model (Stoughton et al., 2001) is shown. This model is used often to

benchmark marine seismic-imaging algorithms. A high velocity (4500 m/s) salt body on the right represents a common imaging challenge. In black, two particular points of interest, \mathbf{x}_1 and \mathbf{x}_2 , are shown (offset 1 km). The solid line S denotes the boundary with source locations. Every twentieth source location is marked by a square, and selected source locations are numbered. These should be distributed with sufficient density such that the wavefields are not aliased after sorting the data into point-of-interest gathers. Outgoing (i.e., radiation or absorbing) boundary conditions (Clayton and Engquist, 1977) are applied just outside the surface, enclosing the points of interest to truncate the computational domain.

Forward simulations were carried out for all of the source locations on the boundary using an elastic FD code (Robertsson et al., 1994), and the waveforms were stored at a large number of points distributed regularly throughout the model. Because we are dealing with the 2D elastodynamic-wave equation, at least two forward simulations must be carried out for each source location: one for each point-force source in mutually orthogonal directions. Here, we also directly computed the response for the special deformation-rate tensor sources, but the equivalent traction data could have been obtained also by spatial filtering of the particle-velocity point-of-interest gathers (see the section on boundary conditions and Appendix A). Since the FD-modeling code is based on a velocity-stress formulation, in the following particle velocity, Green's tensors are used and the interferometric Green's functions are computed after taking the time derivative of the interferometric-modeling equation (equation 10). Again, results are shown in the time domain.

Figure 6 shows the first 4 s of $\dot{g}_{11}(\mathbf{x}_1, \mathbf{x}')$ (i.e., the horizontal component of particle velocity in \mathbf{x}_1 resulting from horizontal point-force sources at location \mathbf{x}' on the boundary) for all boundary sources. For reference, several sources on the boundary have been numbered in Figure 5 (the numbering increases clockwise from just below the free surface on the right). As explained in the section on boundary conditions, no sources are required along the free surface.

An interesting feature of the data, to which we will return later, occurs approximately between sources 200–475 and between sources 1800–2200. These sources are located in the near surface of the sedimentary column, just beneath the water layer. The Pluto model includes many randomly positioned, near-surface scatterers, representing complex near-surface heterogeneity that is often observed in nature. Within these two source ranges, it is clear that all coherent arrivals are followed by complicated codas that are superposed, resulting in a multiply scattered signal that builds with time.

When all components of the Green's tensor and the equivalent traction data have been retrieved for the two points of interest \mathbf{x}_1 and \mathbf{x}_2 , the gathers are crosscorrelated and summed according to the equivalent interferometric-modeling equation for particle velocity. Note that even before numerical integration, this requires summation of crosscorrelation gathers since Einstein's summation convention for repeated indices is used (e.g., in equation 10).

Figure 7a shows the integrand of the interferometric-modeling equation for particle velocity (in the time domain) for the $\dot{g}_{11}(\mathbf{x}_2, \mathbf{x}_1)$ component of Green's tensor between the two points of interest \mathbf{x}_1

and \mathbf{x}_2 . Note how the strongly scattered coda previously identified in Figure 6 affect both negative and positive time lags in the crosscorrelation. In Figure 7b, the Green's function $\dot{g}_{11}(\mathbf{x}_2, \mathbf{x}_1)$ resulting from direct summation of the crosscorrelation traces in Figure 7a along the horizontal direction is shown. Note the emergence of the time symmetry (across $t = 0$ s) from the nonsymmetric crosscorrelations. The intercorrelation Green's function is time-symmetric instead of antisymmetric, as predicted by equation 10, because particle-velocity Green's functions were used in the example instead of particle-displacement Green's functions.

In Figure 8, the four components of the particle-velocity Green's tensor computed using the new method (in blue) are compared to a directly computed reference solution (in green). The $\dot{g}_{11}(\mathbf{x}_2, \mathbf{x}_1)$ component in Figure 8a was shown already in Figure 7b. Note the good match between the directly computed reference solutions and the

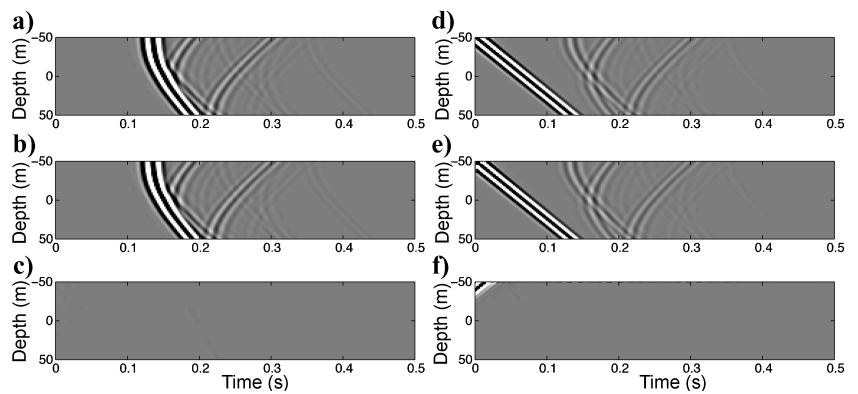


Figure 4. Comparison of Green's functions computed with the interferometric-modeling method and a reference solution for the crosswell-transmission and -reflection setting in Figure 2 with a single source fixed at $[-50, -50]$. (a) Reference solution (transmission), (b) interferometric solution (transmission), and (c) difference ($\times 10$). (d) Reference solution (reflection), (e) interferometric solution (reflection), and (f) difference ($\times 10$). Note the mismatch in (f) for coincident source-receiver; this is because the interferometric solution is diffraction-limited.

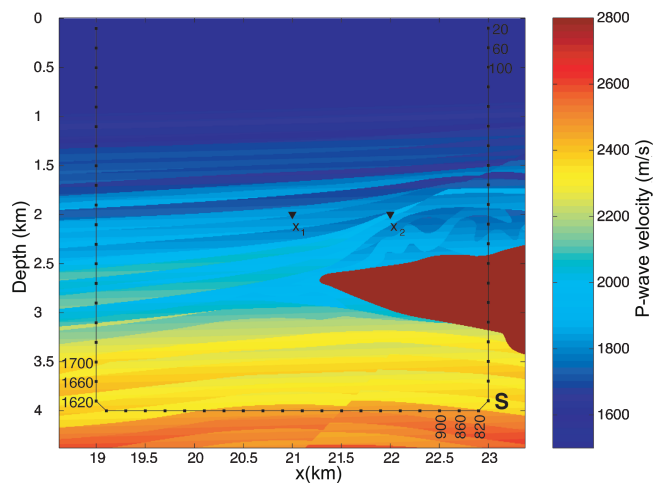


Figure 5. P-wave velocity of a 2D elastic marine-seismic model. The color scale is clipped to display weak velocity contrasts (P -wave velocity of salt is 4500 m/s). The model is bounded by a free surface on top and by absorbing boundary conditions on the remaining sides. Every twentieth source on the surrounding surface S is marked by a dot.

Green's functions computed using the new method, even at late times. The waveforms have been scaled and clipped to show the match in more detail. Some numerical noise at acausal time lags (i.e., before arrival of the direct wave) can be seen clearly. This noise probably is caused by a slight undersampling of the shear wavefield, because the computational parameters have been set rather tightly to minimize computational cost. Note how the different source-radiation patterns are reproduced accurately by the new modeling method; Figure 8a and b show more P-wave energy (e.g., the first significant arrival), which is consistent with a point-force source in the horizontal direction and the second point of interest at the same depth level, whereas Figure 8c and d show more S-wave energy because of the maximum in S-wave radiation in the horizontal direction by a point-force excitation in the vertical direction.

INTERPRETATION OF THE CROSSCORRELATION GATHER

The time series in Figure 7 bear little resemblance to the final Green's function in Figure 8. Equation 10 sums signals such as those in Figure 7 along the horizontal axis and hence relies on the delicate constructive and destructive interference of time-reversed waves back-propagating through the medium, recombining and undoing the scattering at every discontinuity to produce the Green's function. In Figure 7, each column represents the set of all waves propagating from point x_1 to a particular location on the boundary, correlated with the Green's functions from a source at that location to x_2 . Thus, each column represents the Huygens' contribution of a particular boundary source to point x_2 , when the time-reversed wavefield is applied as a boundary condition. Some of the energy propagating from x_1 to this boundary source may pass through x_2 before being recorded, and therefore has part of its path in common with waves emitted from x_2 in the same direction. The traveltimes associated with such identical parts of the path are eliminated in the crosscorrelation, and the remaining traveltimes correspond to an event in the Green's

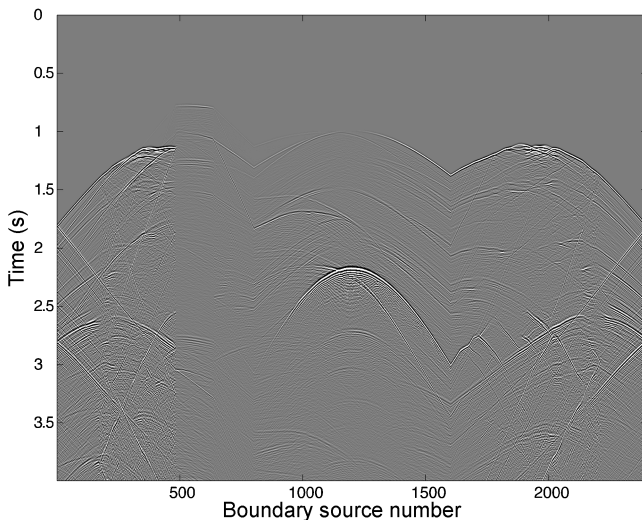


Figure 6. Point-of-interest gather for the left point in Figure 5 showing $\dot{g}_{11}(x_1, x')$, the horizontal component of particle velocity in the point of interest caused by individual horizontal point-force sources on the boundary. This is one of four required particle-velocity Green's-function gathers, computed in the initial phase, needed in the construction of all Green's functions involving that point.

function from x_1 to x_2 . Similarly, some waves emitted from x_2 may travel to the boundary-source location via x_1 and have a common section of path between x_1 and the boundary source. Again, travel-time on the common section will be eliminated and give rise to the same event in the Green's function from x_1 to x_2 , but at negative times. Note that the directions involved with such overlapping paths for positive and negative times in general are not parallel, because they are related to propagation of energy to the boundary through the background structure of the whole model (hence, one or the other may not even exist for the same boundary source). Hence, waves at positive and negative times are reconstructed differently, even though the final Green's function constructed is identical. All energy in the crosscorrelations corresponding to waves that do not pass from x_1 through x_2 , or vice versa, is eliminated by destructive interference through summation of the columns. This process of constructive and destructive interference is discussed in detail by Snieder (2004) and Snieder et al. (2006) using the method of stationary phase.

COMPUTATIONAL ASPECTS

We now discuss some computational aspects of the new modeling method. First, an estimate of the number of floating-point operations

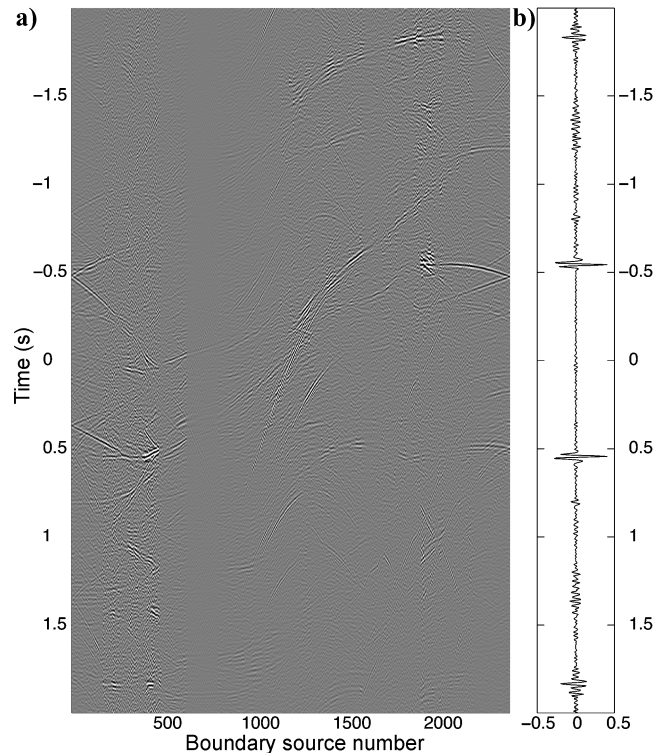


Figure 7. Green's-function intercorrelation gather (weighted) for the two points shown in Figure 5. The low correlation amplitude for boundary sources 620-800 corresponds to the shadow of the salt body. (b) Interferometric Green's function, $\dot{g}_{11}(x_1, x_2, -t) + \dot{g}_{11}(x_1, x_2, t)$, (blue) computed by direct summation of the crosscorrelations in panel (a) along the horizontal direction, compared to a directly computed reference solution (green). Note the emergence of time symmetry from the asymmetric crosscorrelations. The reconstructed Green's function is symmetric, rather than antisymmetric (as predicted by equation 10), because particle-velocity Green's functions were used instead of particle displacement as in the theory.

(flops) is derived for both the initial and intercorrelation phase and compared to the cost of a sequence of conventional FD computations. Then memory and storage implications are highlighted. In Table 1, parameters and variables mentioned in the computational discussion are summarized.

In the following, we ignore the cost of modeling the response to the second source type (i.e., the dipole or deformation-rate tensor sources). As explained in detail in Appendix A, the gradient (or traction) can be computed from the pressure (or particle velocity) through a spatial-filtering procedure as applied to the point-of-interest gathers. The cost of this type of spatial filtering is typically insignificant compared to the FD simulations.

The cost of the initial phase and direct computation

Both direct computation and the initial phase of the new method, while consisting of a sequence of conventional FD simulations, have a computational cost that is directly proportional to the cost of a single FD simulation, C_{FD} . Typically, $C_{FD} \sim aN_T N_X^d$, where N_T is the number of timesteps, N_X is the number of gridpoints in each of d dimensions, and a is the number of flops required for the evaluation of the discrete temporal and spatial derivatives (e.g., $a = 22$ for a typical acoustic 2D FD code). When the data are computed directly, on the order of N_M FD simulations are required (where N_M is the minimum of the number of source and receiver locations considered in the modeling), whereas in the initial phase of the new method at least N_S FD runs need to be carried out (where N_S is the number of source locations on the boundary).

For the new modeling method, however, the simulation time T must be longer than in a conventional FD simulation: Energy that is time-reversed must be recorded on the surrounding surface (in the equivalent reciprocal experiment). In the following, we assume that this doubles the simulation time for the new method. Defining a quantity q , where $q = 1$ for acoustic and $q = d$ for elastodynamic problems, and in the typical case that we are interested in all the components of the Green's tensor, we find for direct computation and the initial phase of the new method

$$C_{CONV} = qN_M C_{FD}, \quad (12)$$

$$C_{INIT} = 2qN_S C_{FD}. \quad (13)$$

The cost of looking up a Green's function

Although the initial phase constitutes the bulk of the computations, the cost of looking up a Green's function cannot simply be ignored, especially when the number of Green's functions that is looked up is large. For each Green's function, at least N_S crosscorrelations and summations must be computed and often more.

On the other hand, in the second, intercorrelation phase of the new method, the strict spatio-temporal sampling requirements of a typical, full-waveform modeling method (as governed by nu-

merical accuracy and the Courant criterion) can be relaxed to Nyquist criteria. For a typical acoustic 2D FD code with second-order accuracy in time and fourth-order accuracy in space, it can be shown

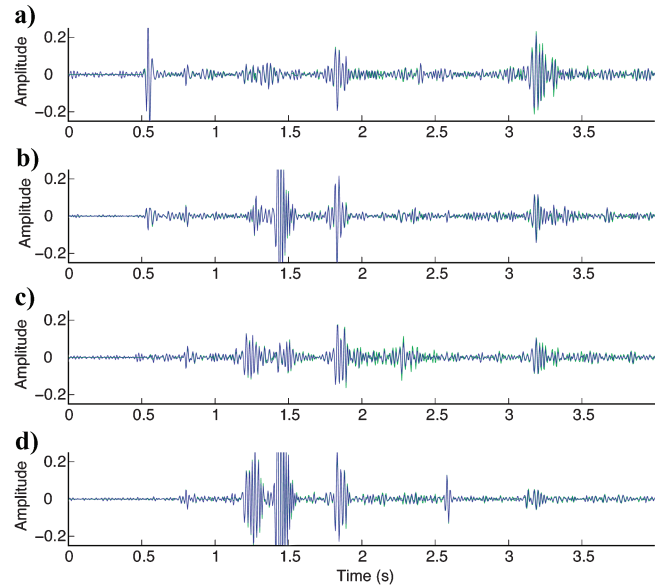


Figure 8. Components of the particle-velocity Green's tensor $\dot{\mathbf{g}}(\mathbf{x}_2, \mathbf{x}_1)$ computed by summation of weighted intercorrelation gathers using the new method (blue) compared to reference solutions computed using a conventional FD method (green). (a) $\dot{g}_{11}(\mathbf{x}_2, \mathbf{x}_1)$, (b) $\dot{g}_{12}(\mathbf{x}_2, \mathbf{x}_1)$, (c) $\dot{g}_{21}(\mathbf{x}_2, \mathbf{x}_1)$, (d) $\dot{g}_{22}(\mathbf{x}_2, \mathbf{x}_1)$. For details see text.

Table 1. Variables mentioned in the computational discussion.

Parameter	Description	Units
a	Number of operations to evaluate the discrete temporal and spatial derivatives	flops
c	Number of crosscorrelations for a single component of Green's tensor	dimensionless
d	Dimension of the modeling	dimensionless
q	Number of source components	dimensionless
C_{FD}	Cost of a single finite-difference run	flops
C_{FFT}	Cost of a combined FFT of two padded, real-valued traces	flops
C_{GREEN}	Cost of a single Green's function intercorrelation	flops
C_{INIT}	Cost of the initial phase in the new method	flops
C_{CONV}	Cost of a conventional sequence of FD simulations	flops
C_{NEW}	Cost using the new methodology to compute Green's functions	flops
N_X	Number of gridpoints along a typical dimension	dimensionless
N_T	Number of timesteps in the initial FD computations	dimensionless
$N_{T'}$	Number of timesteps in the intercorrelation phase	dimensionless
N_S	Number of source locations on the boundary	dimensionless
N_{GF}	Number of Green's function intercorrelations	dimensionless
N_M	Minimum number of conventional sources or receivers	dimensionless

that the ratio of the number of samples N_T in the initial phase to the number of samples $N_{T'}$ in the intercorrelation phase can be as large as 30. Thus, the cost of looking up a Green's function in the intercorrelation phase is reduced substantially by abandoning the oversampling.

In addition, waveforms modeled in the initial phase are stored in the frequency domain in anticipation of the crosscorrelations in the intercorrelation phase. This avoids having to recompute the Fourier transform (FT) of point-of-interest gathers when computing several Green's functions involving the same point of interest. To avoid end effects, the traces are padded with $N_{T'}$ zeros. Transforming a waveform to the frequency domain using a fast Fourier transform (FFT) therefore takes on the order of

$$C_{FFT} \approx N_{T'} \log_2(N_{T'} + 1) \quad (14)$$

flops, where $N_{T'}$ is twice the number of time samples in the desired (one-sided) final seismogram, and we have made use of the fact that the FFT of two real traces can be computed at once.

The number of crosscorrelations, c , that need to be computed for a boundary-source location depends on the type of wave equation (i.e., scalar or vector) and the spatial dimensionality of the problem, d . For an acoustic problem, there is only a single, scalar quantity and this does not increase with the spatial dimensionality. Therefore, $c = 2$, the number of terms in the integrand in equation 11. For an elastic problem, the implicit Einstein summation (for repeated indices) in equation 10 and the two terms in the integrand lead to $c = 2d$. The acoustic and elastic cases can be written in the same form, using the quantity q defined above: $c = 2q$. Complex multiplication of the positive frequencies for all source locations on the boundary and the c crosscorrelations requires $6cN_S N_{T'}$ operations. Complex addition of the c crosscorrelation gathers requires $2(c - 1)N_S N_{T'}$ operations. Multiplying the crosscorrelation gathers with the (varying) weighting factor along the boundary requires $2N_S N_{T'}$ operations. Summing the weighted crosscorrelations for all source locations requires $2(N_S - 1)N_{T'}$ flops. Thus, the total number of flops required for the intercorrelation of a single component of Green's tensor is approximately

$$C_{GREEN} \approx (8c + 2)N_S N_{T'} + C_{FFT}, \quad (15)$$

where C_{FFT} relates to the final inverse FFT. Note that C_{FFT} can typically be neglected, because in most cases of interest $(8c + 2)N_S \gg \log_2(N_{T'} + 1)$. In Table 2, c is computed for 2D and 3D acoustic and elastic modeling.

Table 2. Number of floating-point operations (flops) per gridpoint and timestep in 2D and 3D acoustic and elastic FD modeling.

Parameter	Acoustic		Elastic	
	2D	3D	2D	3D
a	22	32	50	102
q	1	1	$d(=2)$	$d(=3)$
$c(=2q)$	2	2	4	6

Comparison of direct computation and the new method

To make an exact comparison between direct computation and the new method means that one already has chosen a particular source and receiver geometry. In many cases, such as survey evaluation and design and full-waveform seismic inversion, this is simply not possible, and therefore the new method enables the full potential of such applications. In other applications, such as straightforward simulation of synthetic data, one intrinsically limits the uses of the data by deciding on a geometry upfront (e.g., by choosing the source or receiver depth(s) when generating a towed marine synthetic-seismic data set). Nevertheless, it is instructive to assess the relative efficiency of the two methods when a given set of Green's functions must be computed.

Assuming that we are interested in all d^2 components of the Green's tensor and that N_{GF} Green's functions are looked up, the cost of the new method compared to a sequence of conventional FD simulations follows directly from equations 12, 13, and 15:

$$C_{CONV} = qN_M C_{FD}, \quad (16)$$

$$C_{NEW} = 2qN_S C_{FD} + q^2 N_{GF} C_{GREEN}. \quad (17)$$

From these equations, it is not immediately clear that the new method is always more efficient than direct computation. For instance, in the case that one is interested in only Green's functions between a single point and a set of other points, the initial computational burden clearly makes the new method inefficient. In the other extreme case, where one is interested in all combinations of Green's functions between a large number of points, N_M , the new method is also less efficient, because the number of Green's functions to be looked up, N_{GF} , is proportional to the square of N_M . In such a case, equations 16 and 17 are a straight line through zero and a vertically offset parabola, as a function of N_M , respectively, and, at best, there may be a region where the new method is more computationally efficient.

On the other hand, in applications where Green's functions between a large number of points interior to a medium are desired, but where there are no common source or receiver points, the upfront value of the new method is obvious. In such a case, a separate conventional FD simulation is required for each Green's tensor, and hence, $N_{GF} = N_M$. In this case, equations 16 and 17 are a straight line through zero and a vertically offset straight line, as a function of N_M , respectively, and the new method becomes more efficient beyond the intersection point of the two lines. No other existing method could offer full waveforms at comparable computational cost.

Memory and storage

Assuming that a standard, isotropic, elastic FD method is used (e.g., not relying on domain decomposition), the amount of run-time memory required for storage of the $(d/2)(d + 3)$ field quantities (e.g., v_i and σ_{ij}), and three medium parameters (e.g., ρ , λ , and μ) is at least $4[(d/2)(d + 3) + 3]N_x^3$ bytes (for a heterogeneous medium and calculations carried out in single precision). We note that for a medium size of $N_x = 1000$, a 3D elastic problem will require on the order of 45 Gbytes of primary memory. This number grows considerably for even more complex media (e.g., anisotropic), and the computations therefore typically rely on large shared-memory machines or heavily parallelized algorithms running on clusters with high-performance connections. Using our methodology, we compute a table of all point-of-interest gathers using high-end computa-

tional resources. The computations in the intercorrelation phase, on the other hand, would be performed on much smaller machines, because they require a substantially smaller amount of primary memory and because they require only a subset of the intercorrelation table to be exported. We have shown how the point-of-interest gathers with Green's functions constitute a common component of all Green's functions in the medium through equation 10.

SIMULTANEOUS SOURCES: LIMITS OF ENCODING AND DECODING

We also investigated exciting all of the boundary sources simultaneously by encoding the source signals using pseudonoise sequences (Fan and Darnell, 2003) and with simultaneous sources distributed randomly in the medium (Derode et al., 2003) as two alternative ways to reduce the number of sources, and hence, the computational cost of the initial forward-modeling phase. Such approaches have been investigated in attempts to speed up conventional FD simulations, although in surprisingly few published studies. Recent experimental evidence in passive imaging; however, using techniques based on interferometry and time reversal seems to suggest that such an approach would be highly feasible for the new modeling method. For instance, Wapenaar and Fokkema (2004) and Derode et al. (2003) show that, when the sources surrounding and inside the medium consist of uncorrelated noise sequences, their autocorrelation tends to a delta function, and terms involving crosscorrelations between the different noise sequences can be ignored. However, it is well known in the field of communications analysis that Welch's bound (Welch, 1974) poses a fundamental limit to the quality of separation of such pseudonoise sequences of a given length, when emitted simultaneously. In Appendix B, it is shown that, when making no assumptions about the Green's function, the signal-to-interference (from the unwanted crosscorrelations between the encoding sequences) ratio in the final modeled seismogram is proportional to $\sim \sqrt{N}$, where N is the length of the sequences. Thus, the signal-to-interference ratio only improves as the square root of the sequence length. Note that the number of sequences required, the so-called family size M (equal to the number of boundary sources: $M = N_s$), does not influence the signal-to-interference ratio. A similar expression was derived recently by Snieder (2004), using a statistical approach to explain the emergence of the ballistic (direct wave) Green's function through an ensemble of scatterers with uncorrelated positions.

Although in principle and in real-life experiments it is possible to reduce such interference by time/event averaging—where data are modeled for free and all we have to do is listen longer (Snieder 2004)—in synthetic modeling of Green's functions, it is exactly the modeling itself that is expensive. Therefore the use of pseudonoise sequences for the purpose of interferometric, simultaneous-source FD modeling is probably limited. In all explored cases, the limits of separation caused relatively high-noise levels compared to the equivalent FD effort using the direct method described above.

DISCUSSION

Whereas traditional approximate-modeling methods typically impose restrictions with respect to the degree of heterogeneity in the medium of propagation or neglect high-order scattering, the new time-reversal modeling methodology allows us instead to compromise on noise level, while maintaining high-order scattering and full

heterogeneity in the medium. Recent experimental and theoretical work indicates that time-reversed imaging is robust with respect to perturbations in the boundary conditions (Snieder and Scales, 1998; Derode et al., 2003). For cases where the wave propagation is heavily dominated by multiple scattering, even a single source may be sufficient to excite all wavenumbers in the model, and hence to refocus essential parts of a time-reversed signal (Draeger and Fink, 1999). Even when not all wavenumbers are excited by a single source, such as in the examples above, it may be possible to reduce substantially the number of sources and still recover essential parts of the signal. van Manen et al. (2005) showed that even for as few as one-sixteenth of the original number of sources, they were able to reproduce amplitude and phase of an arrival of interest fairly accurately, but with an increased noise level. Clearly, the required number of sources will depend on the application. For many applications, the possibility to trade off signal-to-noise ratio to central processing unit (CPU) time without compromising on medium complexity or high-order scattering will be another attractive property of the new method.

We anticipate that the new methodology also will have a significant impact on inversion. For example, Oristaglio (1989) has shown that the Porter-Bojarski equation (similar to equation 10) forms the basis for an inverse-scattering formula that uses all the data. He proved that a three-step imaging procedure, consisting of back propagation of receiver and source arrays followed by temporal filtering, gives the scattering potential within the Born approximation. His formula relies on complete illumination of a (3D) scattering object from a surface surrounding the object, as our modeling method does.

Interestingly, the method provides exactly those Green's functions required for direct evaluation of higher-order terms in the Neumann-series solution to multiple scattering. Consider perturbing an inhomogeneous background model (e.g., by adding multiple, isotropic point scatterers). In such a case, computation of the interscatterer Green's functions in the background medium may not be trivial, and the new method provides such Green's functions efficiently and flexibly. Note that we do not have to specify even beforehand in which regions of the model we want to perturb or to add the scatterers. Rose (2002) argues that focusing, combined with time reversal, is the physical basis of exact, inverse scattering and derives the Newton-Marchenko equation from these two principles.

The new method also provides a flexible way to compute spatial derivatives of the intercorrelation Green's functions with respect to both source and receiver coordinates for any region in the model, provided the points of interest are spaced closely enough in the initial modeling phase. This makes it straightforward to consider other types of sources and receivers, such as pure P - and S -wave sources and receivers (see, e.g., Wapenaar and Haimé (1990); Robertsson and Curtis (2002); Wapenaar (2004)). Alternatively, in cases where the medium is relatively well known, but where the objective is to track some kind of nonstationary source or receiver within the volume, computationally cheap spatial derivatives also may be a significant advantage.

CONCLUSION

We have shown how the elastodynamic representation theorem can be used to time-reverse a wavefield in a volume, and how, using a second set of Green's functions, the time-reversed wavefield may be computed at any point in the interior. We emphasized the relationship between time reversal, interferometry, holography, and reciprocity theorems of the correlation type. By invoking reciprocity, we

arrived at an expression that is suitable for interferometric modeling of wave propagation and suggested an efficient two-stage modeling scheme, whereby, in an initial phase, the model is illuminated from the outside using a sequence of conventional forward-modeling runs and, in a second phase, Green's functions between arbitrary points in the volume can be computed using only crosscorrelations and summation (numerical integration). The method was illustrated in detail using an acoustic, isotropic, point-scattering example and applied to a region of the elastic Pluto model. A physical description of the crosscorrelation gathers was given, and the computational aspects were discussed. The limitations of source encoding and decoding were discussed also. Finally, implications for modeling and inversion were suggested. We expect that the new method may change significantly the way we approach modeling and inversion of the wave equation in the future.

ACKNOWLEDGMENTS

We thank the associate editor Deyan Draganov, Andrey Bakulin, and two unknown reviewers for their insightful comments. This work was supported by an EU Marie Curie Industry Host Fellowship Grant under the 5th framework program.

APPENDIX A

COMPUTATION OF THE GRADIENT BY SPATIAL FILTERING

It is well known that when the wavefield on a boundary satisfies outgoing (i.e., radiation or absorbing) boundary conditions, the wavefield and its gradient (or traction) are related directly. For example, Holvik and Amundsen (2005) derive the following expressions in the frequency-wavenumber (ω, \mathbf{k}) domain that relate the upgoing components of particle velocity $\mathbf{V}^{(up)}(\mathbf{k})$ of a plane wave propagating with horizontal slowness $\mathbf{p} = (\mathbf{k}/\omega)$ to the upgoing traction $\mathbf{T}^{(up)} \times (\mathbf{k})$ across a horizontal array of receivers (sources):

$$\mathbf{T}^{(up)}(\mathbf{k}) = \mathbf{L}_{TV}(\mathbf{k})\mathbf{V}^{(up)}(\mathbf{k}), \quad (\text{A-1})$$

where the particle velocity and traction vector are defined as

$$\mathbf{V}^{(up)} = (V_1^{(up)}, V_2^{(up)}, V_3^{(up)})^T \quad (\text{A-2})$$

$$\mathbf{T}^{(up)} = (T_1^{(up)}, T_2^{(up)}, T_3^{(up)})^T \quad (\text{A-3})$$

and T denotes transposed. The 3×3 matrix $\mathbf{L}_{TV}(\mathbf{k})$ is derived as (Holvik and Amundsen, 2005):

$$\mathbf{L}_{TV} = \frac{\rho\omega}{k_\phi} \begin{pmatrix} k_{z,\alpha} - \frac{k_y^2}{k_\beta^2}(k_{z,\alpha} - k_{z,\beta}) & \frac{k_x k_y}{k_\beta^2}(k_{z,\alpha} - k_{z,\beta}) & k_x(1 - 2k_\beta^{-2}k_\phi) \\ \frac{k_x k_y}{k_\beta^2}(k_{z,\alpha} - k_{z,\beta}) & k_{z,\alpha} - \frac{k_x^2}{k_\beta^2}(k_{z,\alpha} - k_{z,\beta}) & k_y(1 - 2k_\beta^{-2}k_\phi) \\ -k_x(1 - 2k_\beta^{-2}k_\phi) & -k_y(1 - 2k_\beta^{-2}k_\phi) & k_{z,\beta} \end{pmatrix}. \quad (\text{A-4})$$

In equation A-4, k_x and k_y are the components of the wavenumber vector parallel to the array of receivers (sources); $k_r = (k_x^2 + k_y^2)^{1/2}$ is the length of the wavenumber vector, and $k_{z,\alpha} = (k_\alpha^2 - k_r^2)^{1/2}$ and $k_{z,\beta} = (k_\beta^2 - k_r^2)^{1/2}$ are the P - and S -wavenumbers perpendicular to the array of receivers (sources), respectively, with $k_\alpha = (\omega/\alpha)$ and k_β

$= (\omega/\beta)$ the P - and S -wavenumbers. In addition, an auxiliary quantity $k_\phi = k_r^2 + k_{z,\alpha}k_{z,\beta}$ has been defined.

Similarly, for acoustic waves propagating in a single direction across an array, the pressure $P(\mathbf{k})$ and its gradient $\nabla P(\mathbf{k})$ are related through

$$\frac{\partial P}{\partial n} \equiv \mathbf{n} \cdot \nabla P = ik_{z,\alpha}P, \quad (\text{A-5})$$

where \mathbf{n} is the normal to the array and i is the imaginary unit. Note that these relations depend on material properties and require that the medium is (locally) laterally homogeneous.

Thus, equations A-1–A-5 allow us to calculate the outgoing traction or pressure gradient associated with the modeled particle velocity or pressure on the surface surrounding the medium, because absorbing boundaries were included right outside the enclosing boundary during the modeling.

The implementation of equations A-1–A-5 is straightforward when the wavefield is recorded (or emitted) on a linear array of regularly spaced receivers (sources) embedded in a homogeneous medium. In that case, the point-of-interest gathers can be directly transformed to the frequency-wavenumber domain, and the matrix multiplication carried out explicitly before the components of the resulting traction vector are inverse-Fourier transformed to the space-frequency domain.

Alternatively, when the medium is laterally varying or the array of receivers (sources) is curved, equation A-1 can be implemented by designing spatially compact filters that approximate the terms of \mathbf{L}_{TV} (or, in the acoustic case, $i\omega q_\alpha$) and filtering the data in the space-frequency domain. Such an approach has been used in, for instance, the seabed seismic setting to decompose the wavefield measured at the seabed into upgoing and downgoing P - and S -waves (Røsten et al., 2002; van Manen et al., 2004) and is based on solving a linear least-squares problem with (in)equality constraints to find a small number of spatial-filter coefficients with a wavenumber spectrum that best matches the spectrum of the analytical expression. Because the analytical expressions (equations A-4 and A-5) are functions of frequency, this optimization is carried out separately for each frequency. The laterally varying seafloor properties are accommodated by designing such compact filters for the particular seafloor properties that are present at each receiver location. These filters are applied then to the point-of-interest gathers in the space-frequency domain by space-variant convolution.

Note that the filter coefficients must be optimized only once for a particular model and can be reused for all Green's functions that are computed in the intercorrelation phase. This approach was tested on acoustic data computed for the Pluto model (modeled with $\beta = 0$ m/s) and gave good results.

APPENDIX B

THE WELCH BOUND AND LIMITS TO ENCODING USING PSEUDONOISE SEQUENCES

In communications analysis, the problem of encoding and decoding signals using pseudonoise sequences and its limits are well known. In particular, Welch (1974) has shown that for any family of M (unit energy) sequences $\{a_n^{(i)}\}$, $i = 0, \dots, M-1$, $n = 0, \dots, N-1$ of length N , a lower bound on the maximum (aperiodic) cross-correlation or off-peak autocorrelation is

$$C_{max} = \max\{C_{am}, C_{cm}\} \geq \sqrt{\frac{M-1}{M(2N-1)-1}} \quad (\text{B-1})$$

where C_{am} and C_{cm} are the maximum off-peak autocorrelation and maximum crosscorrelation values defined by

$$C_{am} = \max_i \max_{1 < \tau \leq N-1} |C_{i,i}(\tau)|$$

$$C_{cm} = \max_{i \neq j} \max_{0 < \tau \leq N-1} |C_{i,j}(\tau)|,$$

and $C_{i,j}$ is the discrete aperiodic correlation function of the sequences $a_n^{(i)}$ and $a_n^{(j)}$ defined as

$$C_{i,j}(\tau) = \begin{cases} \sum_{n=0}^{N-1-\tau} a_n^{(i)} a_{n+\tau}^{(j)}, & 0 \leq \tau \leq N-1 \\ \sum_{n=0}^{N-1+\tau} a_{n-\tau}^{(i)} a_n^{(j)}, & -N+1 \leq \tau < 0 \\ 0, & |\tau| \geq N. \end{cases}$$

Note that the Welch bound (equation B-1) holds without reference to a particular type of sequence set (e.g., maximal, Kasami or Gold sequences (Fan and Darnell, 2003)). This means that when we encode signals using sequences of any such family, superpose the encoded signals, and subsequently decode using crosscorrelation, there will be some point in the decoded output where the interference between the original data sequences is at least C_{max} . We can estimate the best possible performance that can be expected (without making any questionable assumptions about the uncorrelatedness of the Green's functions from boundary sources to points of interest) by looking at the rms expected signal-to-interference ratio when all members $a_n^{(i)}$ of the sequence set simply are added, and the result r_n is autocorrelated. Thus, we have

$$r_n = \sum_i a_n^{(i)} \quad (\text{B-2})$$

and the corresponding autocorrelation C_r ,

$$C_r(\tau) = \sum_{n=0}^{N-1-\tau} r_n r_{n+\tau}, \quad 0 \leq \tau \leq N-1, \quad (\text{B-3})$$

which, using equation B-2 can be written

$$C_r(\tau) = \underbrace{\sum_i \sum_{n=0}^{N-1-\tau} a_n^{(i)} a_{n+\tau}^{(i)}}_{C_D(\tau)} + \underbrace{\sum_{i \neq j} \sum_{n=0}^{N-1-\tau} a_n^{(i)} a_{n+\tau}^{(j)}}_{C_C(\tau)} \quad (\text{B-4})$$

The first term denotes the diagonal, or signal term $C_D(\tau)$, whereas the second term $C_C(\tau)$ denotes the cross terms related to the (unwanted) interference between the different codes and contains a double summation.

Equation B-4 mimics the structure of the interferometric-modeling equations (equations 10 and 11): When the boundary source signals are encoded using pseudonoise sequences and excited simultaneously, it is their superposition (convolved with the Green's function) that is recorded in the points of interest. And when calculating the Green's function, decoding, crosscorrelation, and summation are implicit in a direct correlation (just as in a typical retrieval of the

Green's function from uncorrelated noise sources). Thus, as long as we assume that the Green's functions from the boundary to the points of interest do not influence the signal-to-interference ratio, an estimate of the ratio can be found by analyzing equation B-4. This is done by comparing the expected magnitude of the first term to the magnitude of the second term. Since the diagonal term consists of a sum of the autocorrelations of the sequences, its magnitude is maximum at zero lag ($\tau = 0$) and equal to the family size M :

$$C_D(0) = \sum_i \sum_{n=0}^{N-1} a_n^{(i)} a_n^{(i)} = M, \quad (\text{B-5})$$

because the signals are unit energy. The expected value of the second term is calculated actually by Welch as part of his derivation of equation B-1. In fact, Welch's original statement is basically a lower bound on the rms value of a family of unit-energy signals:

$$C_{rms} \geq \sqrt{\frac{M-1}{M(2N-1)-1}}, \quad (\text{B-6})$$

and because $C_{max} \geq C_{rms}$, equation B-1 follows. Thus, the Welch bound gives the rms value of each of the terms within the double sum in $C_C(\tau)$. Note that the sign of each of these $M(M-1)$ terms is not specified directly through the Welch bound. The only thing we can say about the sign is that its expected value is zero when the DC component of the sequences vanishes and the sequences are (in the ensemble average) uncorrelated. Thus, we estimate the magnitude of the term $C_C(\tau)$ by calculating the variance of

$$C_C(\tau) = \pm \underbrace{C_{rms} \pm C_{rms} \pm C_{rms} \dots}_{M(M-1) \text{ terms}}, \quad (\text{B-7})$$

which simply is

$$\langle C_C(\tau) \rangle^{1/2} = \sqrt{M(M-1)} C_{rms}, \quad (\text{B-8})$$

and the ratio of the signal term to the interference term becomes

$$\frac{C_D(0)}{\langle C_C(\tau) \rangle^{1/2}} \approx M \sqrt{\frac{M(2N-1)-1}{M(M-1)^2}}. \quad (\text{B-9})$$

When both the sequence length N and the family size M are much larger than one, this becomes

$$\frac{C_D(0)}{\langle C_C(\tau) \rangle^{1/2}} \approx \sqrt{2N}. \quad (\text{B-10})$$

Thus, the signal-to-interference ratio improves as the square root of the sequence length.

REFERENCES

- Amundsen, L., T. Røsten, J. O. A. Robertsson, and E. Kragh, 2005, Rough-sea deghosting of streamer seismic data using pressure gradient approximations: *Geophysics*, **70**, V1–V9.
- Bakulin, A., and R. Calvert, 2004, Virtual source: new method for imaging and 4D below complex overburden: 74th Annual International Meeting, SEG, Expanded Abstracts, 2477–2480.
- , 2006, The virtual source method: Theory and case study: *Geophysics*, this issue.
- Bojarski, N. N., 1983, Generalized reaction principles and reciprocity theorems for the wave equations, and the relationship between the time-advanced and time-retarded fields: *Journal of the Acoustical Society of America*, **74**, 281–285.
- Cassereau, D., and M. Fink, 1992, Time-reversal of ultrasonic fields—Part

- III: Theory of the closed time-reversal cavity: Institute of Electrical and Electronic Engineers Transactions on Ultrasonics, Ferroelectrics, and Frequency Control **39**, 579–592.
- , 1993, Focusing with plane time-reversal mirrors: an efficient alternative to closed cavities: Journal of the Acoustical Society of America, **94**, 2373–2386.
- Clayton, R., and B. Engquist, 1977, Absorbing boundary conditions for acoustic and elastic wave equations: Bulletin of the Seismological Society of America **67**, 1529–1540.
- de Hoop, A. T., 1988, Time-domain reciprocity theorems for acoustic wave fields in fluids with relaxation: Journal of the Acoustical Society of America, **84**, 1877–1882.
- , 1995, Handbook of radiation and scattering of waves: Academic Press Inc.
- Derode, A., E. Larose, M. Tanter, J. de Rosny, A. Tourin, M. Campillo, and M. Fink, 2003, Recovering the Green's function from field-field correlations in an open scattering medium (L): Journal of the Acoustical Society of America, **113**, 2973–2976.
- Derode, A., P. Roux, and M. Fink, 1995, Robust acoustic time reversal with high-order multiple scattering: Physical Review Letters, **75**, 4206.
- de Rosny, J., and M. Fink, 2002, Overcoming the diffraction limit in wave physics using a time-reversal mirror and a novel acoustic sink: Physical Review Letters, **89**, 124301.
- Draeger, C., and M. Fink, 1999, One-channel time-reversal in chaotic cavities: Theoretical limits: Journal of the Acoustical Society of America, **105**, 611–617.
- Fan, P., and M. Darnell, 2003, Sequence design for communications applications: Research Studies Press.
- Fokkema, J. T., and P. M. van den Berg, 1993, Seismic applications of acoustic reciprocity: Elsevier Science Publishing Company, Inc.
- Foldy, L. L., 1945, The multiple scattering of waves: Physical Review, **67**, 107–119.
- Groenenboom, J., and R. Snieder, 1995, Attenuation, dispersion and anisotropy by multiple scattering of transmitted waves through distributions of scatters: Journal of the Acoustical Society of America, **98**, 3482–3492.
- Hokstad, K., R. Mittet, and M. Landrø, 1998, Elastic reverse time migration of marine walkaway vertical seismic profile data: Geophysics, **63**, 1685–1695.
- Holvik, E., and L. Amundsen, 2005, Elimination of the overburden response from multicomponent source and receiver seismic data, with source designation and decomposition into PP-, PS-, SP-, and SS-wave responses: Geophysics, **70**, 43–59.
- Mittet, R., 1994, Implementation of the Kirchhoff integral for elastic waves in staggered-grid modeling schemes: Geophysics, **59**, 1894–1901.
- Oristaglio, M. L., 1989, An inverse scattering formula that uses all the data: Inverse Problems, **5**, 1097–1105.
- Porter, R. P., 1969, Image formation with arbitrary holographic type surfaces: Physics Letters, **29A**, 193–194.
- , 1970, Diffraction-limited, scalar image formation with holograms of arbitrary shape: Journal of the Optical Society of America, **60**, 1051–1059.
- Rickett, J. E., and J. F. Claerbout, 2000, Calculation of the acoustic solar impulse response by multi-dimensional spectral factorization: Solar Physics, **192**, 203–210.
- Robertsson, J. O. A., J. O. Blanch, and W. W. Symes, 1994, Viscoelastic finite-difference modeling: Geophysics, **59**, 1444–1456.
- Robertsson, J. O. A., and C. H. Chapman, 2000, An efficient method for calculating finite-difference seismograms after model alterations: Geophysics, **65**, 907–918.
- Robertsson, J. O. A., and A. Curtis, 2002, Wavefield separation using densely deployed three-component single-sensor groups in land surface-seismic recordings: Geophysics, **67**, 1624–1633.
- Robertsson, J. O. A., and E. Kragh, 2002, Rough-sea deghosting using a single streamer and a pressure, gradient approximation: Geophysics, **67**, 2005–2011.
- Rose, J. H., 2002, Imaging of complex media with acoustic and seismic waves: Time reversal, focusing and exact inverse scattering, in M. Fink, ed., Topics in applied physics: Springer-Verlag Berlin, **84**, 97–105.
- Røsten, T., D. van Manen, J. O. A. Robertsson, and L. Amundsen, 2002, Optimal nonrecursive and recursive spatial filters for demultiple of OBS data: 72nd Annual International Meeting, SEG, Expanded Abstracts, 1022–1025.
- Schuster, G. T., 2001, Theory of daylight/interferometric imaging: Tutorial: 63rd Annual International Conference and Exhibition, EAGE, Extended Abstracts, Session A-32.
- Snieder, R., 2002, Scattering and inverse scattering in pure and applied science, in R. Pike and P. Sabatier, eds., General theory of elastic wave scattering: Academic Press Inc., 528–542.
- , 2004, Extracting the Green's function from the correlation of coda waves: A derivation based on stationary phase: Physical Review E, **69**, 046610.
- Snieder, R., and J. A. Scales, 1998, Time-reversed imaging as a diagnostic of wave and particle chaos: Physical Review E, **58**, 5668–5675.
- Snieder, R., K. Wapenaar, and K. Lerner, 2006, Spurious multiples in seismic interferometry of primaries: Geophysics, this issue.
- Stoughton, D., J. Stefani, and S. Michell, 2001, 2-D elastic model for wavefield investigations of subsalt objectives, deep water Gulf of Mexico: 71st Annual International Meeting, SEG, Expanded Abstracts, 1269–1272.
- van Manen, D., J. O. A. Robertsson, and A. Curtis, 2005, Modeling of wave propagation in inhomogeneous media: Physical Review Letters, **94**, 164301.
- van Manen, D. J., J. O. A. Robertsson, T. Røsten, L. Amundsen, and A. Strømmen-Melbø, 2004, Decomposition and calibration of multicomponent data in the common shot domain: 66th Annual International Conference and Exhibition, EAGE, Extended Abstracts, D-26.
- Wapenaar, C. P. A., and G. C. Haimé, 1990, Elastic extrapolation of primary seismic P- and S-waves: Geophysical Prospecting, **38**, 23–60.
- Wapenaar, K., 2004, Retrieving the elastodynamic Green's function of an arbitrary inhomogeneous medium by cross correlation: Physical Review Letters, **93**, 254301.
- Wapenaar, K., D. Draganov, and J. Thorbecke, 2004, Relations between reflection and transmission responses of three-dimensional inhomogeneous media: Geophysical Journal International, **156**, 179–194.
- Wapenaar, K., and J. Fokkema, 2004, Reciprocity theorems for diffusion, flow and waves: Journal of Applied Mechanics, **71**, 145–150.
- Wapenaar, K., J. Fokkema, and R. Snieder, 2005, Retrieving the Green's function in an open system by cross-correlation: A comparison of approaches (L): Journal of the Acoustical Society of America, **118**, 2783–2786.
- Weaver, R. L., and O. I. Lobkis, 2001, Ultrasonics without a source: Thermal fluctuation correlations at MHz frequencies: Physical Review Letters, **87**, 134301.
- Welch, L. R., 1974, Lower bounds on the maximum cross correlation of signals: Institute of Electrical and Electronics Engineers Transactions on Information Theory, **20**, 397–399.